# Degradation of Diazinon based on photoelectrocatalytic technique using enhanced WO$_3$ nanostructures: Mechanism and pathway

Gemma Roselló-Márquez [a], Ramón Manuel Fernández-Domene [a,b], Rita Sánchez-Tovar [b], Mireia Cifre-Herrando [a], José García-Antón [a,*]

[a] Ingeniería Electroquímica y Corrosión, Instituto Universitario de Seguridad Industrial, Radiofísica y Medioambiental (ISIRYM), Universitat Politècnica de València, C/ Camino de Vera s/n, 46022 Valencia, Spain
[b] Departamento de Ingeniería Química, Universitat de Valencia, Av de les Universitats, s/n, 46100 Burjassot, Spain

## ARTICLE INFO

## ABSTRACT

In this work, a resistant and toxic pesticide called diazinon was degraded through the photoelectrocatalysis (PEC) technique using tungsten oxide (WO$_3$) nanostructures, applying an external bias of 1V$_{Ag/AgCl}$ and simulated solar illumination. For this, WO$_3$ nanostructures have been synthesized using electrochemical anodization in 0.05 M hydrogen peroxide and 1.5 M of different acidic electrolytes: H$_2$SO$_4$, CH$_4$O$_3$S or HNO$_3$. Morphology, composition and crystallinity of the samples were evaluated through Field Emission Scanning Electron Microscopy (FE-SEM), Atomic Force Microscopy (AFM) and Raman Spectroscopy. Then, the photoelectrochemical properties of the samples were analyzed by Photo-Electrochemical Impedance Spectroscopy (PEIS). The conclusion obtained with these studies was that the nanostructures obtained in the CH$_4$O$_3$S-H$_2$O$_2$ electrolyte presented better photo-electrochemical behavior than the others. The degradation process was checked by UV-Visible, and through Ultra High-Performanc liquid Chromatography and Mass Spectrometry (UHPLC-Q-TOF/MS) the courses of the experiments have been controlled and five possible degradation intermediates have been identified. Finally, after 24 h of experiment, 90% degradation efficiency has been achieved, since it has been possible to decrease from 20 ppm to 2 ppm.

## 1. Introduction

Diazinon is an organophosphate pesticide that belongs to the phosphorothioate subfamily. It is an insecticide used in agriculture to control insects in plants, fruits and vegetables. The main physical-chemical properties of this pesticide are: solubility in water of around 60 ppm, dissociation constant (pKa) of 2.6, density of 1.1 g/mL, vapor pressure of 11.97 mPa and Henry's constant of 6.09·10$^{-2}$ Pa·m$^3$/mol [1].

According to the World Health Organization (WHO), this pesticide is classified as moderately dangerous (Class II) since it has an oral LD$_{50}$ for rats of 1250 mg/kg and a dermal LD$_{50}$ of 540–650 mg/kg [2]. The persistence in soil is 90 days, therefore it is characterized by having a medium persistence in the environment. With a solubility of around 60 ppm, it is considered moderately mobile, and therefore it causes great concern for the quality of groundwater and drinking water.

To eliminate this type of emerging pollutants, advanced oxidation processes (AOP) are used, such as electrooxidation, Fenton processes and photoelectrocatalysis (PEC) that combine electrolytic and photocatalytic processes. Photoelectrocatalysis is a type of photocatalysis in which there is a control of the system potential, that is, the illuminated semiconductor (photocatalyst) is exposed to an adequate electrical potential, which allows improving its overall performance. When a semiconductor is illuminated and the electrons and holes diffuse towards the surface, the electrons will reduce the oxidizing species on the surface or in solution (interface), while the holes will oxidize the reducing ones.

Lately, the use of photoelectrocatalytic technique has obtained significant consideration in the environmental discipline due to its capacity to delay the recombination of electron-hole pairs (e$^-_{CB}$/h$^+_{VB}$) and the chance of increasing the useful life of the latter giving as a result, greater efficiency in the degradation processes of organic compounds [3]. This semiconductor acts as a photocatalyst for chemical reactions, absorbing solar radiation and transforming polluting compounds into less harmful ones.

Photoelectrocatalytic processes are carried out in

photoelectrochemical cells, which act as reactors in order to treat contaminated water or to produce energy by photolysis of water [4]. A photoelectrocatalytic cell involves a container to hold the electrolyte, an anode (usually an n-type semiconductor oxide), a metallic cathode, a transparent window that permits the photoelectrode (semiconductor) to be illuminated and the materials to connect electrically both electrodes to potentiostats (when working in potentiostatic mode). Other elements that are often available are a reference electrode and one or more inputs and outputs for gas flow. In addition, a magnetic stirrer and a membrane that splits the anode and cathode sections to avoid the mixture of oxygen and hydrogen gases can also be found [5].

An ideal photoanode must be composed of semiconductor materials which have the following characteristics: (i) suitable bandgap and bands positions, (ii) efficient separation and transport of the charge carriers in the semiconductor, (iii) strong catalytic activity and stability. Adequate and fast reaction kinetics can prevent the accumulation of surface charges, which otherwise would produce an electron-hole recombination.

$WO_3$ is a semiconductor with a bandgap of 2.6 eV, 0.6 eV narrower than that of $TiO_2$, therefore, visible light can be better used with $WO_3$. The upper edge of the valence band of $WO_3$ exceeds the oxidation potential of $H_2O/O_2$, therefore, the photogenerated holes in $WO_3$ are able to oxidize an extensive variety of organic compounds [6]. Another of the virtues of $WO_3$ is its extraordinary photostability in acidic aqueous electrolytes, making it a potent photocatalyst, for example, for the treatment of wastewater polluted by organic compounds [7].

The crystalline structure of $WO_3$ consists of a $ABO_3$ perovskite structure based on $WO_6$ three-dimensional octahedron networks sharing corners. However, the structure of $WO_3$ shows five stable phases (in the temperature range of 900–180 °C) that corresponds to the tetragonal (α-WO3), orthorhombic (β-WO3), monoclinic I (γ-WO3), triclinic (δ-WO3) and monoclinic II (ε-WO3). Observing all the crystalline structures, the monoclinic structure is highly stable, being the most efficient in photoelectrocatalytic applications [8,9].

Therefore, in this work, $WO_3$ nanostructures will be obtained by electrochemical anodization, which will act as a photoanode in diazinon degradation. Diazinon has been degraded using different techniques [10,11], but in this work PEC using $WO_3$ nanostructures will be employed, as it is a promising Advanced Oxidation Process.

During the anodization, the acid used in the electrolyte will be varied in order to improve the nanostructures obtained. Subsequently, these nanostructures will be used to degrade the diazinon using PEC and the possible degradation products will be analyzed using UHPLC-Q-TOF/MS.

## 2. Material and methods

The experimental procedure that has been followed in this work in order to achieve the objectives has been the following.

### 2.1. Materials

Tungsten (W) rods of 99.5% purity, sulfuric acid ($H_2SO_4$), nitric acid ($HNO_3$), methanesulfonic acid ($CH_4O_3S$), hydrogen peroxide ($H_2O_2$), acetic acid HPLC quality ($CH_3COOH$), acetonitrile ($C_2H_3N$), diazinon (analytical standard) employed in this research are commercially available products. Some of them were purchased from Sigma–Aldrich and others from PanReac. All the aqueous solutions were prepared using distilled water.

### 2.2. Synthesis of $WO_3$ nanostructures

$WO_3$ nanostructures were synthetized by electrochemical anodization using three different electrolytes, with $H_2O_2$ 0.05 M in all of them. The first one was sulfuric acid ($H_2SO_4$) 1.5 M. The second one was nitric acid ($HNO_3$) 1.5 M, and finally, the third one was methanesulfonic acid

($CH_4O_3S$) 1.5 M.

Anodization was executed at a constant potential of 20 V using an Elektro-Automatik power source for 4 h, with W rod as the anode and a platinum mesh as the cathode, and the electrolyte temperature was 50 °C. The velocity at which the working electrode (tungsten rod) was rotating was at 375 rpm by using a Rotating Disk Electrode (RDE) [12].

Annealing of the $WO_3$ nanostructures occurred in a flowing air atmosphere using a tubular furnace at 600 °C during 4 h. The heating rate was fixed at 15 °C/min whereas the cooling was carried out at room temperature.

### 2.3. Morphological and structural characterization

The morphology of the nanostructures was analysed by FE-SEM using a Zeiss Ultra 55 microscope at 3 kV, and the surface topography of the nanostructures was evaluated by means of an Atomic Force Microscope (AFM). The images were obtained through the atomic force microscope WITec alpha300A operated at room temperature. AFM measurements have been carried out in contact mode.

Moreover, the crystalline structure was examined using a confocal Raman microscope with a neon laser of 632 nm at 750 μW.

### 2.4. Photoelectrochemical characterization of the $WO_3$ nanostructures

Photoelectrochemical properties were studied using a three-electrode assembly with a platinum mesh as counter electrode and a Ag/AgCl 3 M KCl reference electrode. The samples were electrically connected with a potentiostat (Autolab PGSTAT302N) exposing 0.5 $cm^2$ of active surface. The samples were submerged in 0.1 M $H_2SO_4$ solution. Photoelectrochemical impedance spectroscopy (PEIS) and Mott–Schottky tests were executed under illuminated conditions. PEIS measurements were taken at a potencial of 1 V (10 mV of amplitude) and scanning frequency from 10 KHz down to 10 mHz. Mott–Schottky type measurements were carried out at a frequency of 5 kHz using an amplitude signal of 10 mV and scanning the potential from a value of 0.5 V in the negative direction at a rate of 50 mV/s.

### 2.5. Photoelectrocatalytic degradation

For the photoelectrocatalytic (PEC) degradation analysis, the pesticide diazinon was selected as a target substance to degrade with an initial concentration of 20 ppm. A 500 W xenon lamp was employed to apply the necessary visible light to carry out the experiments under illumination conditions. The distance between the photoreactor and lamp was 30 cm and the visible light intensity was 100 mW/$cm^2$. The degradation of diazinon was performed in a quartz reactor with nanostructures acting as the photoanode, platinum wire used as the counter electrode, and a Ag/AgCl 3 M KCl electrode performing as the reference electrode. The bias potential applied on the photoanode was 1 V (vs Ag/AgCl). All the experiments were carried out with magnetic stirring at room temperature (Scheme is shown in Fig. S1 (Supplementary Material)). The problem solution was studied by registering variations of the absorption spectra in the UV–vis spectra of diazinon using an UV–vis spectrophotometer (Unicam UV/Vis spectrometer UV4) every 30 min and after the measuring the aliquots were returned inside the reactor.

### 2.6. UHPLC-Q-TOF/MS analysis

Chromatographic tests was performed using an Agilent 1290 Infinity HPLC equipment fitted with a C-18 analytical column (Agilent ZORBAX Eclipse Plus C18, 50 mm × 2.1 mm, 1.8 m particle size). 10 μL of each sample were caught in each measurement. Two mobile phases (A and B) were used. Mobile phase A was milli-Q water and mobile phase B was acetonitrile, both with 0.1% acetic acid (v/v). The method used an initial mobile phase composition of 5% of B constant for 3 min. Then, this composition augmented until 10% of B, an finally, it was followed
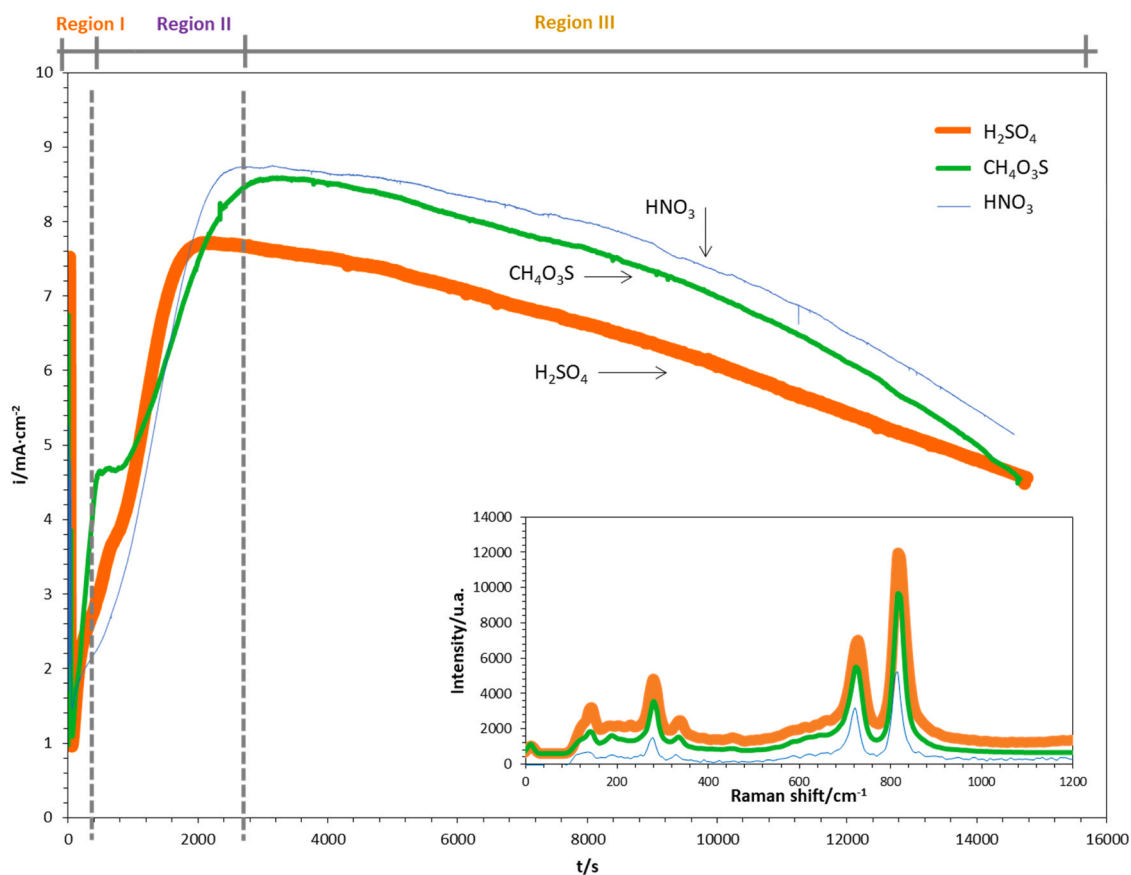
**Fig. 1.** Current density transient recording during anodization of tungsten in different acids as electrolyte. Insets show Raman spectra of annealed samples as an example.

by a linear gradient to 100% B up to 25 min, and kept for 3 min at 100% B. The flow rate was 0.5 mL/min. The HPLC system was coupled to a time-of flight mass spectrometer fitted with an electrospray interface operated in positive or negative ionization mode, employing the next process parameters: capillary voltage 4000 V; nebulizer pressure 40 psi; drying gas flowrate 9 L/min; gas temperature 325 °C; skimmer voltage 65 V; octopole rf 250 V; fragmentor voltage 190 V. LC–MS exact mass spectra were registered across the range of 70–1200 $m/z$ in positive ionization mode.

## 3. Results and discusión

Fig. 1 shows the current density transients during electrochemical anodization of tungsten for all the different type of electrolytes. All the curves show the characteristic trend of the formation of tungsten oxide nanostructures with the three typical regions: (1) formation of a compact tungsten oxide layer [13,14], (2) decomposition of this layer formed in the earlier step due to the hydrogen peroxide and the $H^+$ present in the electrolyte and the applied potential [15,16], and (3) the precipitation of tungstic acids ($WO_3 \cdot H_2O$ and $WO_3 \cdot 2H_2O$) from peroxowolframates in the form of nanostructures [12].

Despite using three different acids with the formation of their respective counter-anions, the curves differ little between them, except for small differences, such as the maximum value reached or the slope, since the shape is very similar. From this first analysis, it is not possible to deduce which acid will be the optimum in the synthesis, which indicates that the nanostructures are being obtained in a similar way. However, with the rest of the characterizations, the differences in morphology, topology, crystal structure and photoelectrocatalytic properties of the nanostructures can be verified.

Raman spectra of the different samples after annealing were similar

even though the acid used during anodization is different. Raman spectra of all samples synthesised in different electrolytes are shown in inset of Fig. 1. The peaks that arise at approximately 125 cm$^{-1}$, 195 cm$^{-1}$, 275 cm$^{-1}$, 715 cm$^{-1}$ and 822 cm$^{-1}$ indicate the presence of crystalline $WO_3$ [17]. These peaks were the result of the vibration of the bending of the crystalline (O-W-O) bonds (both monoclinic and orthorhombic) of $WO_3$ [18].

Again, no significant differences are found between the Raman spectra obtained for the 3 different samples, suggesting that the crystalline structure of all of them was similar and they presented a similar degree of dehydration, since no characteristic bands of amorphous structures are observed.

### 3.1. Morphological characterization WO$_3$ nanostructures

Fig. 2 shows FE-SEM images of the nanostructures obtained with the three different acids, at 1000 and 20,000 magnifications. This morphology is related to the recorded transient of current density, which defined the characteristic behavior of the formation of nanostructures.

Broadly speaking, in the case of the sample anodized in $H_2SO_4$ (Fig. 2a and b) it is observed that very small nanoplates grow in the form of nanofilaments creating a kind of spongy layer. These aggregated nanostructures form clusters in the form of cones or "mountains" as seen in images at 1000 magnifications.

With the use of $CH_4O_3S$ as electrolyte (Fig. 2c and d), nanostructures are obtained with a morphology of tiny nanowires, creating a spongy layer too. The morphology of these very small nanostructures may be associated to the tendency of the bidentate ligand $O_2^{2-}$ to create very robust bonds with tungsten, which makes it difficult for the nanostructures to grow during anodization, as mentioned in other publications [19–21]. However, the morphology of the nanostructures in this
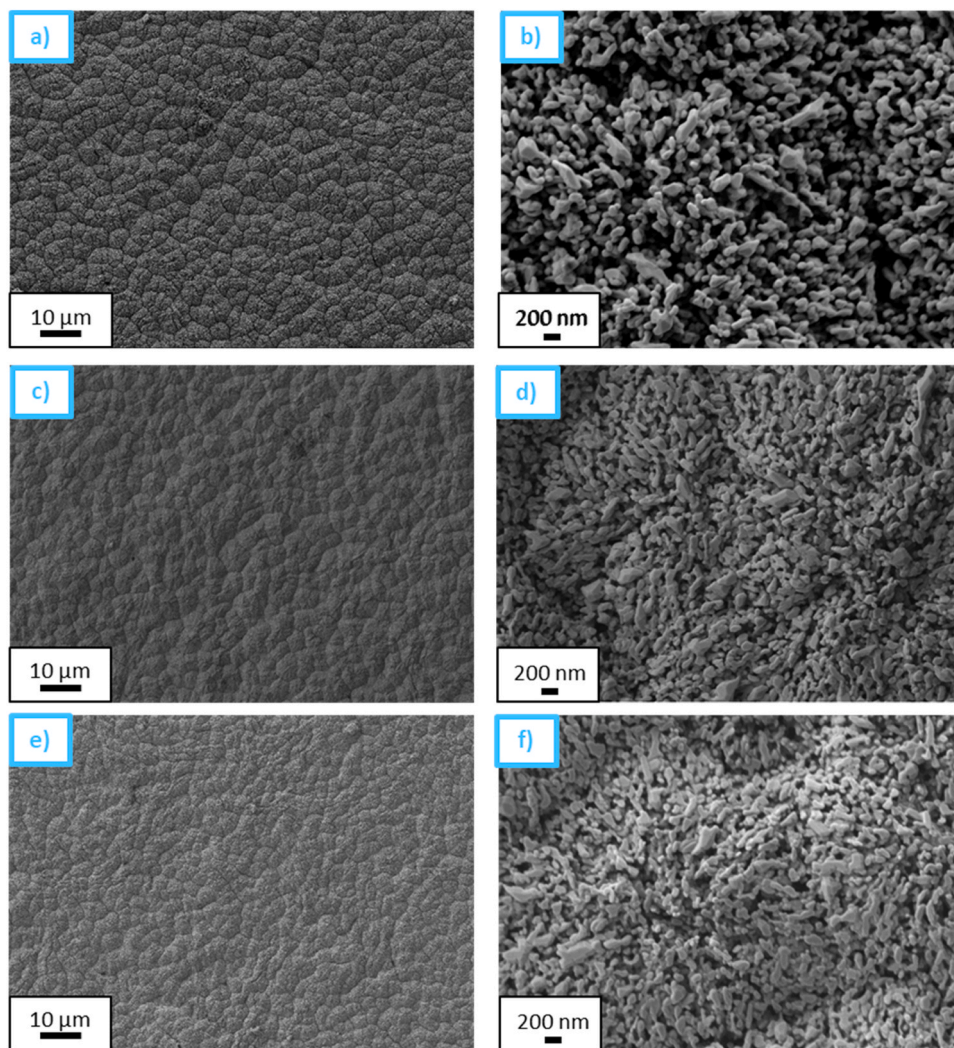
**Fig. 2.** Field Emission Scanning Electron Microscopy (FE-SEM) images of nanostructures obtained with (a) $H_2SO_4$ at 1000 augments, (b) $H_2SO_4$ at 20,000 augments, (c) $CH_4O_3S$ at 1000 augments, (d) $CH_4O_3S$ at 20,000 augments, (e) $HNO_3$ at 1000 augments, (f) $HNO_3$ at 20,000 augments.

case is more uniform than in the case of employing $H_2SO_4$ as electrolyte. The formation of this type of layer, will produce higher current densities [22–24] and consequently, this nanostructure could be more efficient in degrading pesticides than nanowires obtained in $H_2SO_4$.

This can occur due to the high surface area of the nanostructures obtained with $CH_4O_3S$, which allows the effective capture of sunlight and the production of electron-hole pairs. The photogenerated holes exit quickly of the nanostructure and reach the electrolyte. Furthermore, electrons travel to the metal substrate easily due to the low presence of spaces between the nanostructures and making the path less impeded [25,26]. Therefore, the high probability of recombination is reduced [27,28].

The morphological results obtained when using $HNO_3$ in the electrolyte (Fig. 2e and f) are nanostructures similar to those obtained with $H_2SO_4$ where the nanostructures are more compact leading to less porosity, so the properties of these nanostructures should be similar at the samples obtained with $H_2SO_4$. However, the morphology that was obtained was much more disordered, with nanowires appearing in the form of small agglomerates.

Another form to characterize the nanostructures is with the atomic force microscopy (AFM), a technique that shows the topography of the samples. In Fig. 3 the topography of the different samples is showed. As it can be seen in these images, the samples are made up of spherical nanograins of the order of 400 nm in the case of nanowires obtained

with $H_2SO_4$ and $CH_4O_3S$, and the order of 800 nm for those obtained with $HNO_3$, all of them making good contact with each other. The images also manifest a greatly porous organization with conglomerates of grains, which are separated by large irregular gaps that vary between approximately 300 and 600 nm. Tungsten oxide films synthesized with $CH_4O_3S$ are more porous than films made with $HNO_3$, but similar to $H_2SO_4$. This type of structure is regarded crucial for the efficient functioning of photoelectrochemical materials, since it exhibits good charge transfer electrical conductivity [29,30].

In the nanostructures obtained with $H_2SO_4$ and $CH_4O_3S$ a great growth of the nanograins (whitish peaks) can be seen in Fig. 3, while in those obtained with $HNO_3$ they are much less pronounced, giving rise to a lower roughness. The average roughness values of the $WO_3$ films are shown in Fig. 3 with the abbreviation of Sa. The highest value of roughness of the films is shown by the sample synthesized in $CH_4O_3S$, this may be due to the agglomeration of the microcrystals with this acid. In addition, a rougher surface morphology is beneficial for adsorption of organic compounds, so, it is suitable for enhancing photoelectrocatalytic degradation due to a larger surface area [31–33].

The morphology observed in the AFM images is slightly different from that obtained in the FE-SEM images. This is because the AFM works with a confocal microscope and the resolution to see the morphology of the nanostructures is not as high as that of the FE-SEM. Nevertheless, AFM results are very important, since they confirm the greater
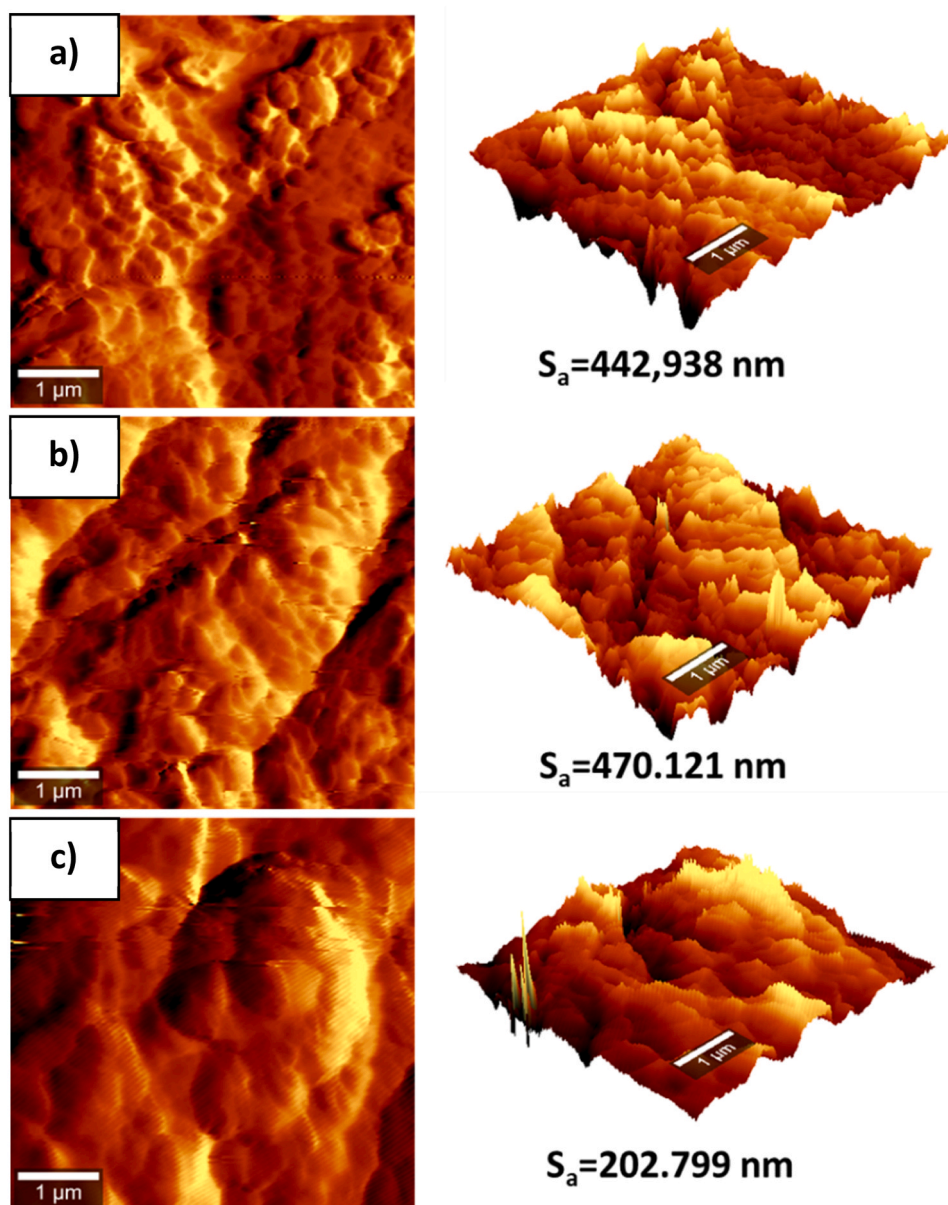
$S_a$=442,938 nm



$S_a$=470.121 nm



$S_a$=202.799 nm

**Fig. 3.** AFM images in two and three dimensions of the nanostructures obtained with (a) $H_2SO_4$, (b) $CH_4O_3S$ y (c) $HNO_3$.

roughness of the sample anodized in the methanesulfonic electrolyte and its superior porosity.

### 3.2. Photoelectrocatalytic characterization of the $WO_3$ nanostructures

In order to analyse the photoelectrochemical characteristics of the three different samples, Photoelectrochemical Impedance Spectroscopy (PEIS) tests were carried out. First of all, a stability test that lasted 30 min was carried out in which the stability of the samples under illumination was evaluated. Then, through PEIS tests, Nyquist diagrams are obtained, from which the photoelectrochemical processes that are occurring can be characterized, and finally, Mott–Schottky analysis were performed. These results are shown in Fig. 4.

From the present study, it can be concluded that the sample synthesized with $CH_4O_3S$ presents better results than the others, since in the Nyquist diagram it is the one that shows the lowest amplitude of the semicircle. The amplitude of the semicircle is directly related to the resistance to charge transfer and therefore, the smaller this amplitude, the lower the resistance will be [34,35]. Therefore, it is expected that

this sample has a better photoelectrochemical behavior than the nanowires obtained with the other acids. These results might be associated to the morphology of the nanostructures since they present a greater contact between them, which improves the interfacial electrochemical and photoelectrochemical transfer [36,37]. The values of the photocurrent density and PEIS show that the nanowires synthetized with $CH_4O_3S$ present the best separation efficiency of photogenerated charge carriers, as well as the fastest electron transport between the electrolyte and the nanostructures [38–41].

Regarding Mott-Schottky tests, the number of defects ($N_D$) of the three different samples has been obtained, being $20.4 \pm 8.6 \cdot 10^{19}$ cm$^{-3}$ in case of the samples obtained for $H_2SO_4$, $52.4 \pm 6.5 \cdot 10^{19}$ cm$^{-3}$ for the samples obtained with $CH_4O_3S$ and $6.51 \pm 0.21 \cdot 10^{19}$ cm$^{-3}$ for those obtained with $HNO_3$. So, the highest value is obtained with nanostructures synthetized with $CH_4O_3S$. This has been seen in the Mott-Schottky plots (Fig. 4c), where the sample anodized in $CH_4O_3S$ electrolyte showed the lowest slope. This slope is inversely proportional to the amount of defects in the nanostructures, and therefore, this sample is the one with the highest number of defects, making it more
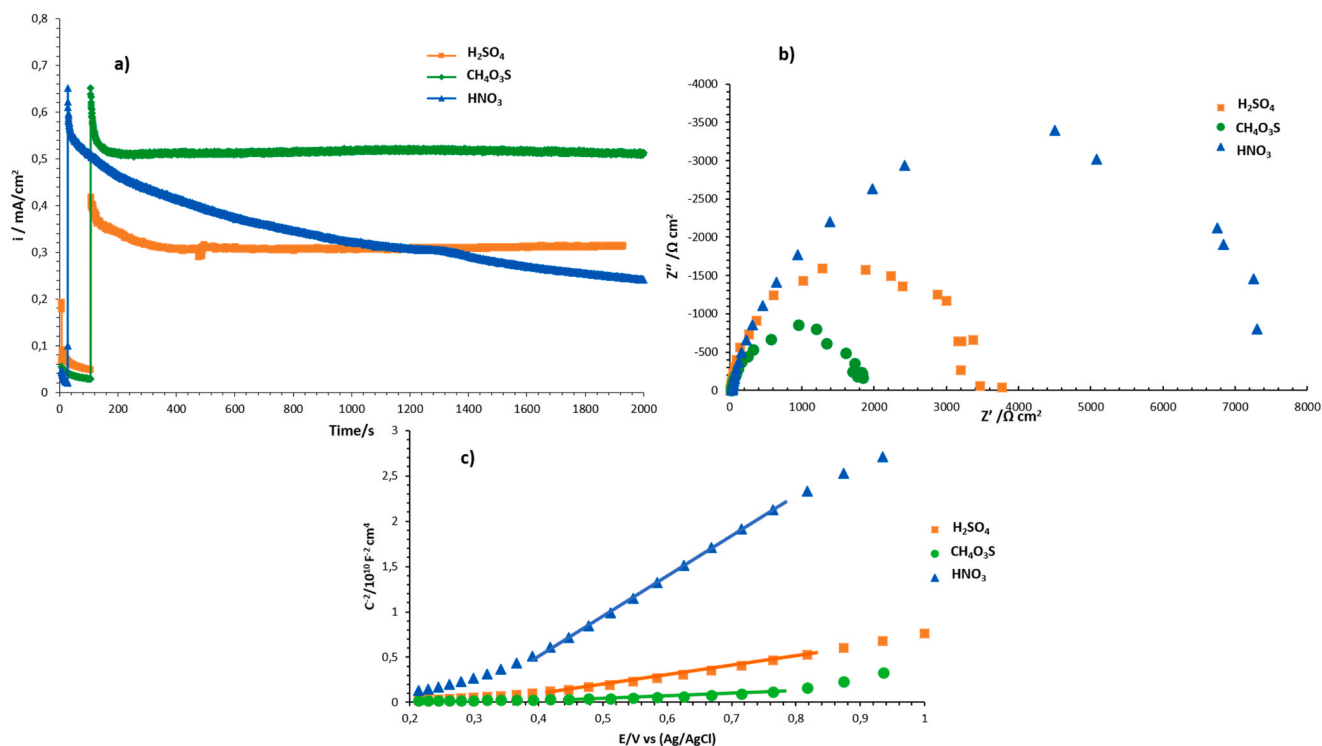
**Fig. 4.** (a) Stability test for 30 min, (b) Nyquist diagram of the different samples and (c) Mott–Schottky plots obtained with different acids.
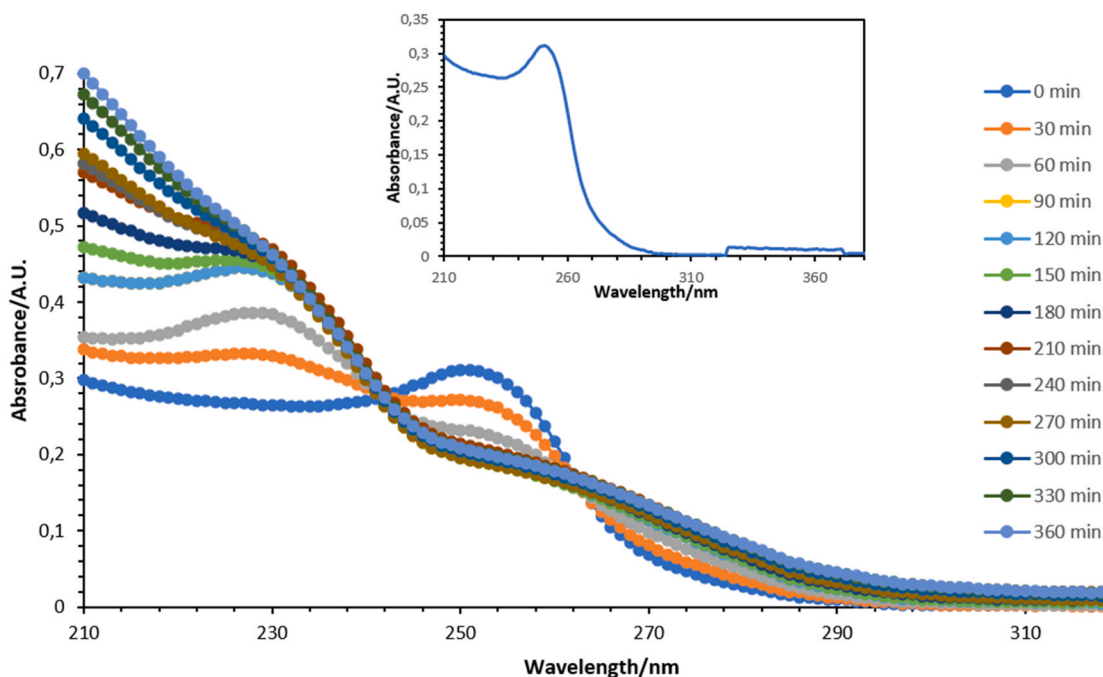


**Fig. 5.** Variation with time of the UV-Vis spectrum of diazinon in PEC degradation. Inset show UV-Vis spectrum of diazinon at 20 ppm.

photocatalytically active [42–44]. Consequently, it can be concluded that these nanostructures are the optimal to be used as photo-electrocatalysts since charge-transfer processes and electronic conductivity are enhanced [45–48].

### 3.3. Photoelectrodegradation of diazinon

Once the optimal sample for its use as photoanode in the degradation of organic compounds had been chosen (nanostructures obtained by

CH$_4$O$_3$S), the photoelectrochemical degradation of the organophosphate pesticide diazinon was carried out. The degradation was followed by both ultraviolet-visible spectroscopy and UHPLC-Q-TOF/MS.

#### 3.3.1. UV absorbance

Fig. 5 shows the UV spectrum of samples taken every half hour during photoelectrochemical degradation. The initial pesticide solution had a concentration of 20 ppm of diazinon in 0.1 M H$_2$SO$_4$. It can be seen that the spectrum of the initial solution of diazinon has a maximum
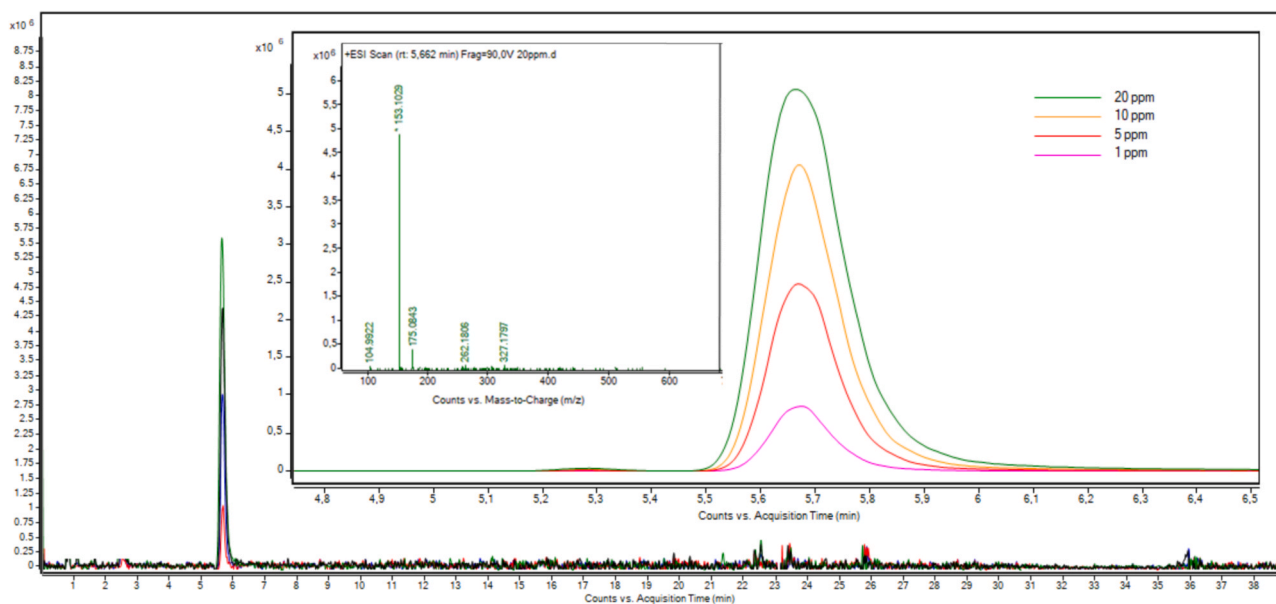
**Fig. 6.** TIC chromatogram of diazinon standards. Insets show a magnification of this peak and its mass spectra.
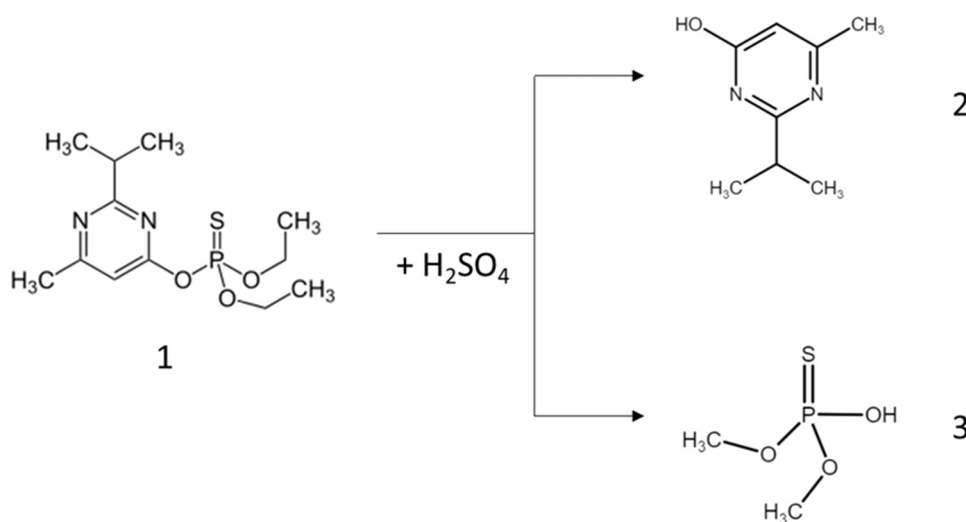


**Fig. 7.** Pathway of Diazinon hydrolysis under acidic conditions.

absorbance band at 250 nm (inset in Fig. 5) which has been associated in the literature with the characteristic diazinon aromatic ring. This peak is related to the excitation of an electron from a π-bonding orbital to an antibonding π* orbital [49] and is usually employed to track the degradation of this organic compound. Moreover, the band observed at 330 nm has been related to n-π* transition referring to the sulfur atom where an electron coming from non-bonding orbital is upgraded to anti-bonding π* orbital [50].

The band at 250 nm progressively decreased with irradiation time until 270 min, where it remained practically constant (Fig. 5). However, a new band emerged with the time at 230 nm, which corresponds to the formation of degradation intermediates, although this band slightly decreased when the experiment ended. This degradation intermediate may be a smaller molecule because of the breakdown of the pesticide through ethanothiol bond or phosphoramidate bond [51], resulting in a smaller and less polar molecule, or the incorporation of auxochromes groups like - OH and –NH$_2$ in the ring [52]. This could be the reason why, at a smaller wavelength, the band emerges to the left, because both

perform as auxochromes.

*3.3.2. UHPLC-Q-TOF/MS analysis*

Subsequently, by UHPLC-Q-TOF/MS tests, the standards and the diazinon samples picked up every hour were evaluated. Firstly, the standards were evaluated to obtain a calibration line (shown in Eq. (1) with a R$^2$ of 0.9914) which will be employed to calculate the concentration of diazinon in the experimental samples. Moreover, in Fig. S2 (Supplementary Material), it can be seen the calibration line.

$$Area \quad (counts) = 3,310,267.7854 \times concentration \tag{1}$$

In Fig. 6, the Total Ion Current (TIC) chromatograms of the diazinon standards at 1 ppm, 5 ppm, 10 ppm and 20 ppm are shown, as well as a zoom in the peak area to analyze better the results and the corresponding spectrum.

However, if the *m/z* value of the spectrum is observed, it does not correspond to the *m/z* of the diazinon (*m/z* = 305.108), since the *m/z* obtained is 153.1029. This *m/z* corresponds to the product 2-isopropyl-
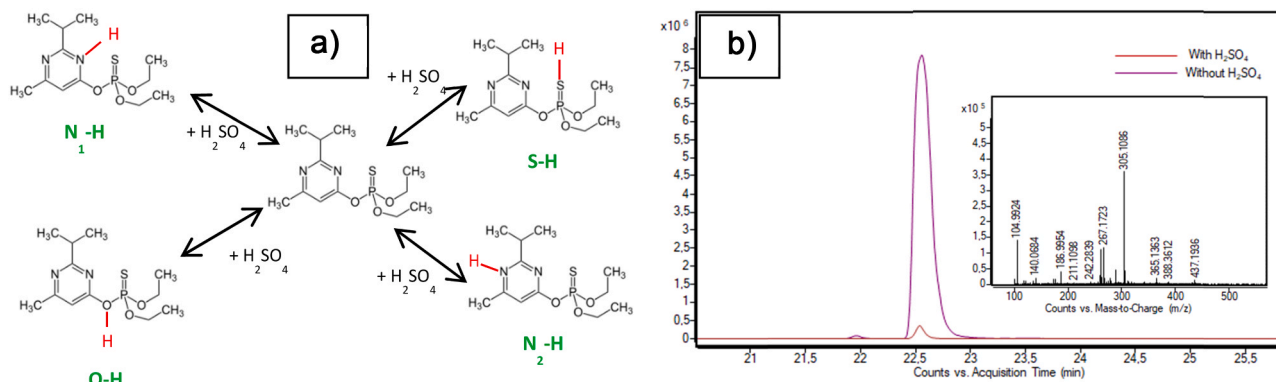
**Fig. 8.** (a) Protonation pathways of Diazinon and (b) Chromatogram of diazinon with and without H$_2$SO$_4$ and its masa's spectra.
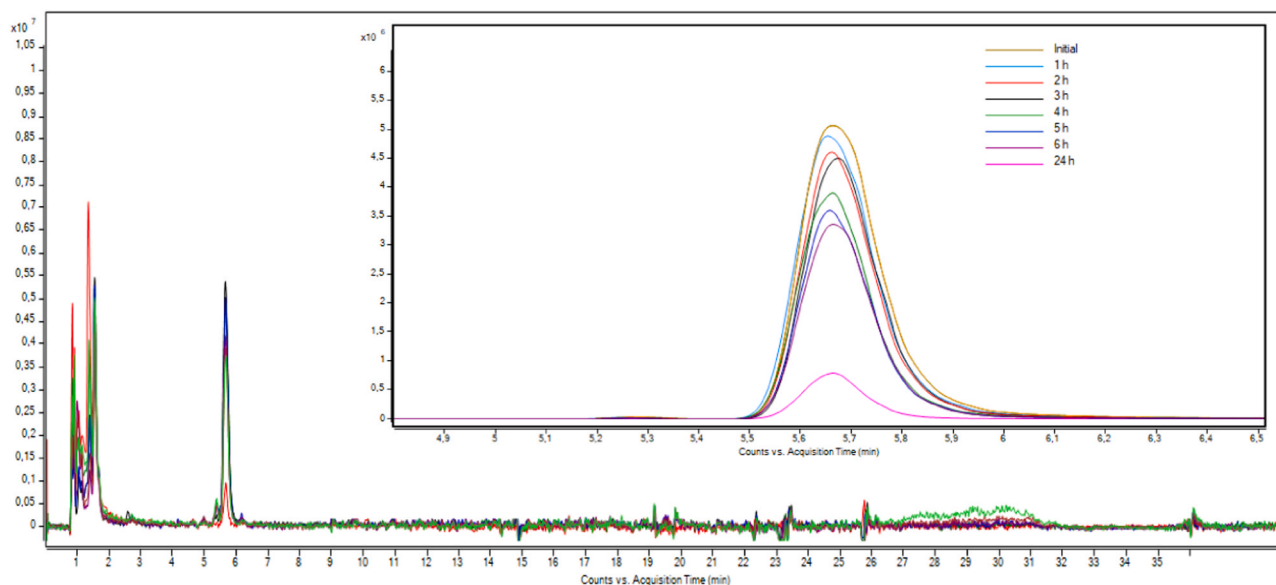


**Fig. 9.** TIC chromatogram of all degraded samples. Inset shows a magnification of the principal peak.

6-methylpyrimidin-4-ol (IMP) [53,54]. This can be explained according to the study by Ku et al. which concluded that IMP (2) and O, O-dimethylphosphorothioate (DETP) (3) were obtained as derivatives of the hydrolysis of diazinon in an acid medium [55], as shown in Fig. 7.

This is mainly because at low pH, the attack on the aromatic carbon and (or) phosphorus could be realized more easily, since H$_2$O, as the softer nucleophile, would be probable to select the attack on the softer carbon site [56,57]. Therefore, in acidic media, a multiplicity of protonation sites occurs, as shown in Fig. 8a). Fig. 8b) shows the difference between the diazinon peak at 20 ppm observed with and without acidic media and its respective spectrum where the *m/z* corresponds to the *m/z* of diazinon. It can be seen that the peak of the diazinon in an acid medium is much smaller than the peak corresponding to the diazinon without an acid medium, since the diazinon has been hydrolyzed when it comes into contact with H$_2$SO$_4$.

The protonation of the diazinon on the aryloxy oxygen, generating O-H, would improve the reaction by providing a better leaving group after attack on the phosphorus. Otherwise, protonation of the nitrogen of the ring of diazinon to give N$_1$-H or N$_2$-H would also generate a more suitable leaving group and therefore could improve the reaction. Protonation at P = S to give S-H would rise the P electrophilicity, improving the attack of nucleophiles on phosphorus. Therefore, hydrolysis in fairly acidic media may be due to as a result of any of these protonations or through the interaction of various simultaneously [55,58]. In conclusion, in a H$_2$SO$_4$ electrolyte, diazinon hydrolyzes rapidly to give IMP and

DETP, so the peak observed in the chromatogram corresponds to IMP instead of diazinon. Therefore, this could be regarded as the first step in PEC diazinon degradation, where IMP and DETP would be the initial species.

Fig. 9 shows the UHPLC-Q-TOF/MS TIC chromatograms of diazinon and its intermediates present in the samples taken every hour. In the magnified chromatogram it can be observed that after 24 h of experiment the pesticide concentration is around 1 ppm. The concentration of IMP present in all samples can be calculated from the calibration line (Eq. (1)). Table 1 shows the concentration of IMP in each samples.

Therefore, the kinetics of diazinon degradation when applying the PEC technique is a pseudo-first order kinetics with the following equation and an R$^2$ of 0.991.

**Table 1**
Concentration of IMP at each time of degradation.

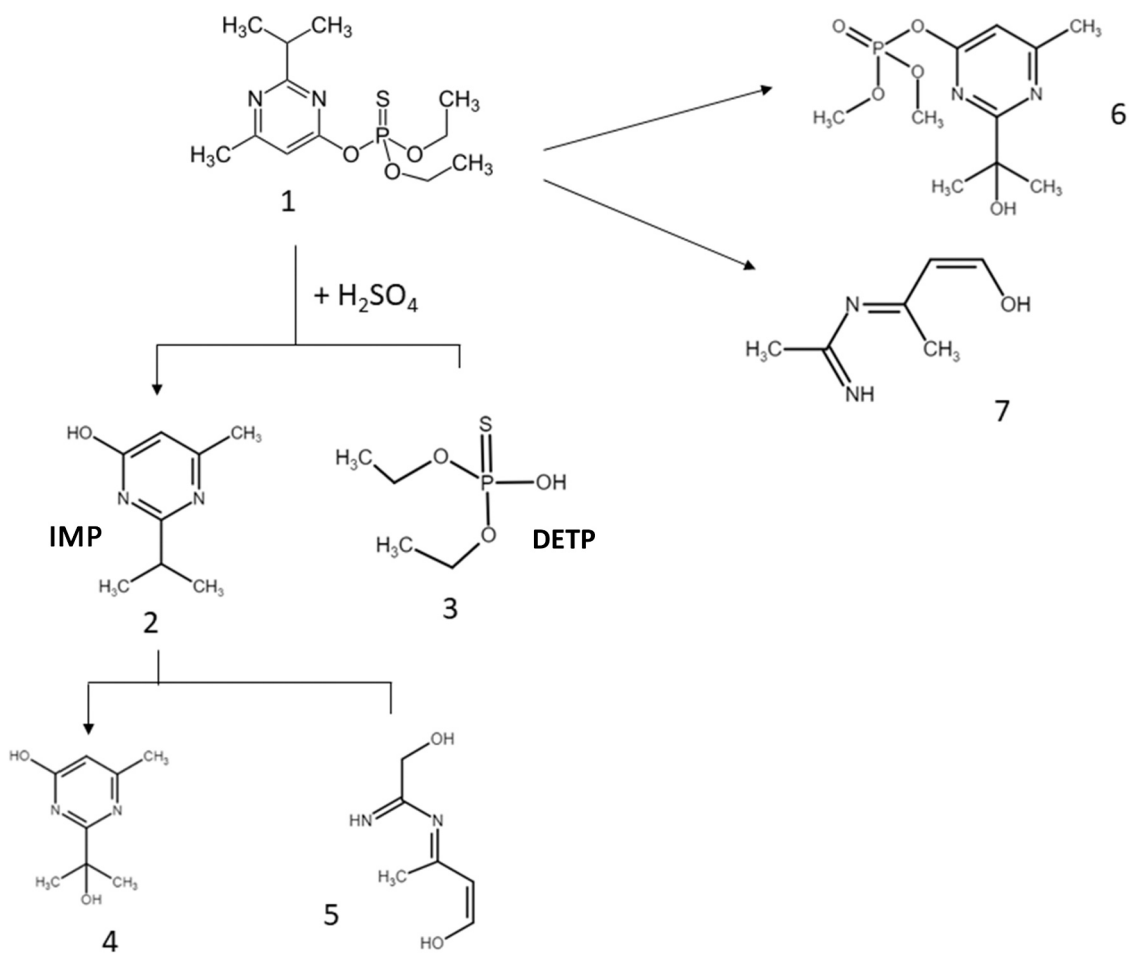| | Area | Concentration (ppm) |
|---|---|---|
| 1 h | 54,680,909.9 | 16.51 |
| 2 h | 48,509,678.5 | 14.65 |
| 3 h | 45,618,361.2 | 13.78 |
| 4 h | 40,668,829 | 12.28 |
| 5 h | 36,600,076.9 | 11.05 |
| 6 h | 35,095,441.8 | 10.60 |
| 24 h | 6,980,753.64 | 2.10 |

**Fig. 10.** Proposed PEC degradation pathway of diazinon.

**Table 2**
Exact mass values and elemental composition of diazinon and its degradation intermediates using UHPLC/MS-Q-TOF analysis.

| Proposed compound | Compound | Molecular formula | Retention time (s) | Observed mass ($[M + H]^+$) |
|---|---|---|---|---|
| **2** | IMP | $C_8H_{13}N_2O$ | 5.68 | 153.1029 |
| **4** | 2-isopropanol-6-methylpyrimidin-4-ol | $C_8H_{13}N_2O_2$ | 5.38 | 169.097 |
| **5** | 2-hydroxy-N-((2E,3Z)-4-hydroxybut-3-en-2-ylidene)acetimidamide | $C_5H_8N_2O_3$ | 0.92 | 144.982 |
| **6** | 1-hydroxyisopropyl diazoxon | $C_{12}H_{22}N_2O_5P$ | 22.32 | 305.12 |
| **7** | N-((2E,3Z)-4-hydroxybut-3-en-2-ylidene)acetimidamide | $C_6H_{10}N_2O$ | 1.55 | 155.046 |

$$\ln\left(\frac{C}{C_0}\right) = -0.0969 \cdot t \qquad (2)$$

where $t$ is in hours (so the kinetic coefficient has units of $h^{-1}$).

From the last chromatogram, degradation intermediates have been identified thanks to literature, as well as the identification of peaks present in that chromatogram. Fig. 10 shows the identified intermediates. The intermediates found, following to other studies that analyzed possible intermediates of the pesticide, are 2-isopropanol-6-methylpyrimidin-4-ol (referred as 4 in Fig. 10) [59] and 1-hydroxyisopropyl diazoxon (referred as 6 in Fig. 10) [53,60]. In both cases, the concentration of the intermediate increases as the degradation time goes forward. However, in the case of 2-isopropanol-6-methylpyrimidin-4-ol (4), this compound practically disappears after 24 h. This may be because once the intermediate is formed, it was degraded into smaller molecules.

Furthermore, from the peaks present in the degradation TIC chromatogram, two new intermediates were identified, such as products 5 (2-hydroxy-N-((2E,3Z)-4-hydroxybut-3-en-2-ylidene)acetimidamide) and 7 (N-((2E,3Z)-4-hydroxybut-3-en-2-ylidene)acetimidamide), shown in Fig. 10. Again, the concentration of compound 5 increases with time, while compound 7 reaches its maximum value after 1 h and subsequently a third part of the maximum concentration is degraded.

The results acquired in Q-TOF measurements are summarized in Table 2. This table shows the molecular formula, retention time and observed mass of each intermediate compound measured in positive ionization mode.

Therefore, according to the identified intermediates, the proposed diazinon degradation route is shown in Fig. 9.

Intermediates 6 and 7 are the degradation products of diazinon that remained in the unhydrolyzed solution (Fig. 11a shows the Extracted Ion Chromatogram (EIC) of the diazinon present in the standards and Fig. 11b shows the chromatogram of all the degraded samples in order to demonstrate that diazinon does not fully hydrolyze when enter in contact with $H_2SO_4$) [61].

If the results obtained with UV-Vis and UHPLC-Q-TOF/MS are compared, it can be assumed that the band at ≈230 nm in ultraviolet
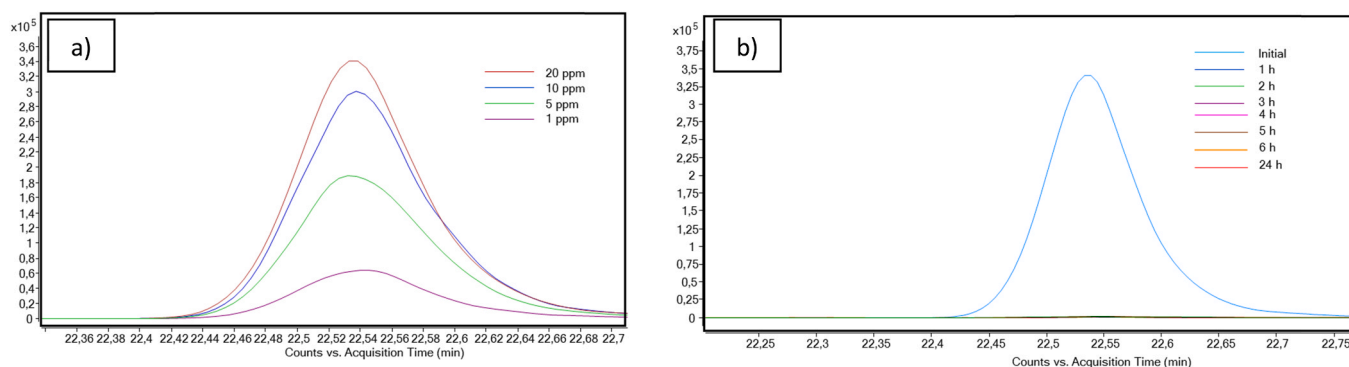
**Fig. 11.** (a) EIC chromatogram of standards of diazinon and (b) EIC chromatogram of diazinon for the degraded simples.

spectrum corresponds to the appearance of species 5 (according Fig. 10). This is due to the new compound is a molecule with a lower polarity and a smaller size and this could be the motive why the band arises shifted to the left.

These results show that the photoanode obtained using $CH_4O_3S$ as electrolyte is an excellent photoelectrocatalyst since it is possible to efficiently degrade the diazinon, resulting in less toxic and harmful compounds with an environmentally friendly process. Therefore, with these excellent results, a promising horizon opens in which to continue investigating in this field of great technological potential, such as the photoelectrochemical degradation technique, and with which great results can be achieved in the environmental area.

## 4. Conclusions

In this work, the electrolyte effect on the anodization of tungsten oxide to obtain nanostructures was investigated with the aim to synthesize the optimal nanostructures for being used as photoelectrocatalyst in the degradation of organic compounds. Results showed that the highest and most stable photocurrent densities were achieved for the nanostructures synthesized with $CH_4O_3S$ as electrolyte. FE-SEM images indicated that this nanostructure showed a porous morphology with nanowires above the surface, which could enhance its photoelectrocatalytic activity since electron-hole separation was improved. Furthermore, AFM tests revealed that the nanostructures obtained by $CH_4O_3S$ present a greater roughness, thus providing an excellent active surface area. Finally, the Mott-Schottky tests pointed out that this sample showed a high number of defects ($N_D$) leading to an improvement in their electrical conductivity.

Moreover, the performances of photoelectrocatalytic degradation of diazinon, using the optimal nanostructures obtained with $CH_4O_3S$, were examined. Based on the HPLC/MS measurements, five degradation intermediates were detected during the PEC degradation, which proposed possible degradation pathways. The obtaining of 1-hydroxyisopropyl diazoxon by the replacement of sulfur by oxygen on the P=S bond through oxidation was the first part of diazinon degradation. Then, the formation of IMP and 2-isopropanol-6-methylpyrimidin-4-ol (4), was the second part of the degradation pathway. The results presented in this study shown that this procedure can be employed to successfully degrade diazinon and decrease its toxicity.

## CRediT authorship contribution statement

**Gemma-Roselló-Márquez:** Methodology, Investigation, Writing paper, **Ramón M. Fernández-Domene:** Conceptualization, Methodology, Resources. **Rita Sánchez-Tovar:** Conceptualization, Methodology, Resources, **Mireia Cifre-Herrando:** Methodology, **José García-Antón:** Supervision.

## Declaration of Competing Interest

The authors declare that they have no known competing financial interests or personal relationships that could have appeared to influence the work reported in this paper.

## Appendix A. Supporting information

Supplementary data associated with this article can be found in the online version at doi:10.1016/j.jece.2021.105371.

## References

[1] M.H. Rasoulifard, M. Akrami, M.R. Eskandarian, Degradation of organophosphorus pesticide diazinon using activated persulfate: optimization of operational parameters and comparative study by Taguchi's method, J. Taiwan Inst. Chem. Eng. 57 (2015) 77–90, https://doi.org/10.1016/j.jtice.2015.05.014.

[2] A.A. Salarian, Z. Hami, N. Mirzaie, S.M. Mohseni, A. Asadi, H. Bahrami, M. Vosoughi, A. Alinejad, M.R. Zare, N-doped TiO2 nanosheets for photocatalytic degradation and mineralization of diazinon under simulated solar irradiation: optimization and modeling using a response surface methodology, J. Mol. Liq. 220 (2016) 183–191, https://doi.org/10.1016/j.molliq.2016.04.060.

[3] V. Cristino, S. Marinello, A. Molinari, S. Caramori, S. Carli, R. Boaretto, R. Argazzi, L. Meda, C.A. Bignozzi, Some aspects of the charge transfer dynamics in nanostructured WO3 films, J. Mater. Chem. A 4 (2016) 2995–3006, https://doi.org/10.1039/c5ta06887h.

[4] M. Nasrollahi, A.A. Pourbabaei, H. Etesami, K. Talebi, Diazinon degradation by bacterial endophytes in rice plant (Oryzia sativa L.): a possible reason for reducing the efficiency of diazinon in the control of the rice stem–borer, Chemosphere 246 (2020), 125759, https://doi.org/10.1016/j.chemosphere.2019.125759.

[5] D.A. Skoog, F.J. Holler, S.R. Crouch, Principios de análisis fundamental, sixth ed., Cengage learning, 2008.

[6] H. Ahmadian, F.S. Tehrani, M. Aliannezhadi, Hydrothermal synthesis and characterization of WO3 nanostructures: effects of capping agent and pH, Mater. Res. Express 6 (2019) 105024, https://doi.org/10.1088/2053-1591/ab3826.

[7] C. Di Valentin, G. Pacchioni, Spectroscopic properties of doped and defective semiconducting oxides from hybrid density functional calculations, Acc. Chem. Res. 47 (2014) 3233–3241, https://doi.org/10.1021/ar4002944.

[8] A. Di Paola, F. Di Quarto, C. Sunseri, Anodic oxide films on tungsten-I. The influence of anodizing parameters on charging curves and film composition, Corros. Sci. 20 (1980) 1067–1078, https://doi.org/10.1016/0010-938X(80)90085-2.

[9] M. Jamali, F. Shariatmadar Tehrani, Effect of synthesis route on the structural and morphological properties of WO3 nanostructures, Mater. Sci. Semicond. Process. 107 (2020), 104829, https://doi.org/10.1016/j.mssp.2019.104829.

[10] B. Ayoubi-Feiz, M.H. Mashhadizadeh, M. Sheydaei, Degradation of diazinon by new hybrid nanocomposites N-TiO2/Graphene/Au and N-TiO2/Graphene/Ag using visible light photo-electro catalysis and photo-electro catalytic ozonation: optimization and comparative study by Taguchi method, Sep. Purif. Technol. 211 (2019) 704–714, https://doi.org/10.1016/j.seppur.2018.10.032.

[11] S. Sajjadi, A. Khataee, N. Bagheri, M. Kobya, A. Şenocak, E. Demirbas, A. G. Karaoğlu, Degradation of diazinon pesticide using catalyzed persulfate with Fe3O4@MOF-2 nanocomposite under ultrasound irradiation, J. Ind. Eng. Chem. 77 (2019) 280–290, https://doi.org/10.1016/j.jiec.2019.04.049.

[12] R.M. Fernández-Domene, R. Sánchez-Tovar, B. Lucas-Granados, G. Roselló-Márquez, J. García-Antón, A simple method to fabricate high-performance nanostructured WO3 photocatalysts with adjusted morphology in the presence of complexing agents, Mater. Des. 116 (2017) 160–170, https://doi.org/10.1016/j.matdes.2016.12.016.

[13] H.L. Lord, W. Zhan, J. Pawliszyn, Fundamentals and applications of needle trap devices, Anal. Chim. Acta 677 (2010) 3–18, https://doi.org/10.1016/B978-0-12-381373-2.00056-9.

[14] R.M. Fernández-Domene, R. Sánchez-Tovar, E. Segura-Sanchís, J. García-Antón, Novel tree-like WO3 nanoplatelets with very high surface area synthesized by anodization under controlled hydrodynamic conditions, Chem. Eng. J. 286 (2016) 59–67, https://doi.org/10.1016/j.cej.2015.10.069.

[15] W. Li, J. Li, X. Wang, S. Luo, J. Xiao, Q. Chen, Visible light photoelectrochemical responsiveness of self-organized nanoporous WO3 films, Electrochim. Acta. 56 (2010) 620–625, https://doi.org/10.1016/j.electacta.2010.06.025.

[16] E. Lassner, W.-D. Schubert, Properties, chemistry, technology of the element, alloys, and chemical compounds, Plenum (1999).

[17] J.Z. Ou, R.A. Rani, S. Balendhran, A.S. Zoolfakar, M.R. Field, S. Zhuiykov, A. P. O'Mullane, K. Kalantar-Zadeh, Anodic formation of a thick three-dimensional nanoporous WO3 film and its photocatalytic property, Electrochem. Commun. 27 (2013) 128–132, https://doi.org/10.1016/j.elecom.2012.11.009.

[18] C. Santato, M. Odziemkowski, M. Ulmann, J. Augustynski, Crystallographically oriented mesoporous WO3 films: synthesis, characterization, and applications, J. Am. Chem. Soc. 123 (2001) 10639–10649, https://doi.org/10.1021/ja011315x.

[19] P. Dias, T. Lopes, L. Meda, L. Andrade, A. Mendes, Photoelectrochemical water splitting using WO3 photoanodes: the substrate and temperature roles, Phys. Chem. Chem. Phys. 18 (2016) 5232–5243, https://doi.org/10.1039/c5cp06851g.

[20] J.Z. Ou, M.Z. Ahmad, K. Latham, K. Kalantar-Zadeh, G. Sberveglieri, W. Wlodarski, Synthesis of the nanostructured WO3 via anodization at elevated temperature for H2 sensing applications, Procedia Eng. 25 (2011) 247–251, https://doi.org/10.1016/j.proeng.2011.12.061.

[21] C. Wang, R. Sun, X. Li, Y. Sun, P. Sun, F. Liu, G. Lu, Hierarchical flower-like WO3 nanostructures and their gas sensing properties, Sens. Actuators B Chem. 204 (2014) 224–230, https://doi.org/10.1016/j.snb.2014.07.083.

[22] R.M. Fernández-Domene, R. Sánchez-Tovar, B. Lucas-Granados, J. García-Antón, Improvement in photocatalytic activity of stable WO3 nanoplatelet globular clusters arranged in a tree-like fashion: influence of rotation velocity during anodization, Appl. Catal. B Environ. 189 (2016) 266–282, https://doi.org/10.1016/j.apcatb.2016.02.065.

[23] C.W. Lai, S. Sreekantan, Fabrication of WO3 nanostructures by anodization method for visible-light driven water splitting and photodegradation of methyl orange, Mater. Sci. Semicond. Process. 16 (2013) 303–310, https://doi.org/10.1016/j.mssp.2012.10.007.

[24] C.J.W. Ng, Synthesis of Tungsten Oxide for Solar Energy Conversion and Water Splitting Applications (PhD Sch.), Chem. Eng. Univ., New South Wales, 2012, pp. 5–10.

[25] Y. Liu, Y. Li, W. Li, S. Han, C. Liu, Photoelectrochemical properties and photocatalytic activity of nitrogen-doped nanoporous WO 3 photoelectrodes under visible light, Appl. Surf. Sci. 258 (2012) 5038–5045, https://doi.org/10.1016/j.apsusc.2012.01.080.

[26] C. Ng, Y.H. Ng, A. Iwase, R. Amal, Influence of annealing temperature of WO3 in photoelectrochemical conversion and energy storage for water splitting, ACS Appl. Mater. Interfaces 5 (2013) 5269–5275.

[27] N. Naseri, Photoresponse enhancing in nanostructured WO3 films by slight change in heating ambient, J. Alloy. Compd. 693 (2017) 871–875, https://doi.org/10.1016/j.jallcom.2016.09.275.

[28] Y. Chai, C.W. Tam, K.P. Beh, F.K. Yam, Z. Hassan, Effects of thermal treatment on the anodic growth of tungsten oxide films, Thin Solid Films 588 (2015) 44–49, https://doi.org/10.1016/j.tsf.2015.04.033.

[29] K.J. Lethy, D. Beena, R. Vinod Kumar, V.P. Mahadevan Pillai, V. Ganesan, V. Sathe, Structural, optical and morphological studies on laser ablated nanostructured WO 3 thin films, Appl. Surf. Sci. 254 (2008) 2369–2376, https://doi.org/10.1016/j.apsusc.2007.09.068.

[30] M. Urbańczyk, E. Maciak, K. Gut, T. Pustelny, W. Jakubik, Layered thin film nanostructures of Pd/WO 3-x as resistance gas sensors, Bull. Polish Acad. Sci. Tech. Sci. 59 (2011) 401–407, https://doi.org/10.2478/v10175-011-0048-4.

[31] K.H. Chung, D.E. Kim, Fundamental investigation of micro wear rate using an atomic force microscope, Tribol. Lett. 15 (2003) 135–144, https://doi.org/10.1023/A:1024457132574.

[32] Y.M. Hunge, M.A. Mahadik, S.S. Kumbhar, V.S. Mohite, K.Y. Rajpure, N. G. Deshpande, A.V. Moholkar, C.H. Bhosale, Visible light catalysis of methyl orange using nanostructured WO3 thin films, Ceram. Int. 42 (2016) 789–798, https://doi.org/10.1016/j.ceramint.2015.08.178.

[33] A. Watcharenwong, W. Chanmanee, N.R. de Tacconi, C.R. Chenthamarakshan, P. Kajitvichyanukul, K. Rajeshwar, Anodic growth of nanoporous WO3 films: morphology, photoelectrochemical response and photocatalytic activity for methylene blue and hexavalent chrome conversion, J. Electroanal. Chem. 612 (2008) 112–120, https://doi.org/10.1016/j.jelechem.2007.09.030.

[34] L. Bertoluzzi, J. Bisquert, Equivalent circuit of electrons and holes in thin semiconductor films for photoelectrochemical water splitting applications, J. Phys. Chem. Lett. 3 (2012) 2517–2522, https://doi.org/10.1021/jz3010909.

[35] B. Klahr, S. Gimenez, F. Fabregat-Santiago, T. Hamann, J. Bisquert, Water oxidation at hematite photoelectrodes: the role of surface states, J. Am. Chem. Soc. 134 (2012) 4294–4302, https://doi.org/10.1021/ja210755h.

[36] T. Zhu, M.N. Chong, Y.W. Phuan, E.S. Chan, Electrochemically synthesized tungsten trioxide nanostructures for photoelectrochemical water splitting: influence of heat treatment on physicochemical properties, photocurrent densities and electron shuttling, Colloids Surf. A Physicochem. Eng. Asp. 484 (2015) 297–303, https://doi.org/10.1016/j.colsurfa.2015.08.016.

[37] R. Levinas, N. Tsyntsaru, M. Lelis, H. Cesiulis, Synthesis, electrochemical impedance spectroscopy study and photoelectrochemical behaviour of as-deposited and annealed WO3 films, Electrochim. Acta 225 (2017) 29–38, https://doi.org/10.1016/j.electacta.2016.12.112.

[38] Y.O. Kim, S.H. Yu, K.S. Ahn, S.K. Lee, S.H. Kang, Enhancing the photoresponse of electrodeposited WO3 film: structure and thickness effect, J. Electroanal. Chem. 752 (2015) 25–32, https://doi.org/10.1016/j.jelechem.2015.05.031.

[39] Q. Mi, R.H. Coridan, B.S. Brunschwig, H.B. Gray, N.S. Lewis, Photoelectrochemical oxidation of anions by WO3 in aqueous and nonaqueous electrolytes, Energy Environ. Sci. 6 (2013) 2646–2653, https://doi.org/10.1039/c3ee40712h.

[40] S. Prabhu, L. Cindrella, O.J. Kwon, K. Mohanraju, Photoelectrochemical and photocatalytic activity of TiO2-WO3 heterostructures boosted by mutual interaction, Mater. Sci. Semicond. Process. 88 (2018) 10–19, https://doi.org/10.1016/j.mssp.2018.07.028.

[41] L.E. Fraga, J.H. Franco, M.O. Orlandi, M.V.B. Zanoni, Photoelectrocatalytic oxidation of hair dye basic red 51 at W/WO 3/TiO2 bicomposite photoanode activated by ultraviolet and visible radiation, J. Environ. Chem. Eng. 1 (2013) 194–199, https://doi.org/10.1016/j.jece.2013.04.018.

[42] Y. Liu, Y. Li, W. Li, S. Han, C. Liu, Photoelectrochemical properties and photocatalytic activity of nitrogen-doped nanoporous WO3 photoelectrodes under visible light, Appl. Surf. Sci. 258 (2012) 5038–5045, https://doi.org/10.1016/j.apsusc.2012.01.080.

[43] K. Siuzdak, M. Szkoda, M. Sawczak, A. Lisowska-Oleksiak, J. Karczewski, J. Ryl, Enhanced photoelectrochemical and photocatalytic performance of iodine-doped titania nanotube arrays, RSC Adv. 5 (2015) 50379–50391, https://doi.org/10.1039/c5ra08407e.

[44] E. Ahmadi, C. Yan, K. Abdul, Z. Lockman, Preparation of anodic nanoporous WO3 film using oxalic acid as electrolyte, J. Alloy. Compd. 704 (2017) 518–527, https://doi.org/10.1016/j.jallcom.2017.02.123.

[45] W. Li, J. Li, X. Wang, J. Ma, Q. Chen, Photoelectrochemical and physical properties of WO3 films obtained by the polymeric precursor method, Int. J. Hydrog. Energy 35 (2010) 13137–13145, https://doi.org/10.1016/j.ijhydene.2010.09.011.

[46] W. Li, P. Da, Y. Zhang, Y. Wang, X. Lin, X. Gong, G. Zheng, WO3 nanoflakes for enhanced photoelectrochemical conversion, ACS Nano 8 (2014) 11770–11777, https://doi.org/10.1021/nn5053684.

[47] J. Zhu, W. Li, J. Li, Y. Li, H. Hu, Y. Yang, Photoelectrochemical activity of NiWO4/WO3 heterojunction photoanode under visible light irradiation, Electrochim. Acta 112 (2013) 191–198, https://doi.org/10.1016/j.electacta.2013.08.146.

[48] J. Georgieva, S. Sotiropoulos, S. Armyanov, N. Philippidis, I. Poulios, Photoelectrocatalytic activity of bi-layer TiO2/WO3 coatings for the degradation of 4-chlorophenol: effect of morphology and catalyst loading, J. Appl. Electrochem. 41 (2011) 173–181, https://doi.org/10.1007/s10800-010-0221-8.

[49] L. Tajeddine, M. Nemmaoui, H. Mountacer, A. Dahchour, M. Sarakha, Photodegradation of fenamiphos on the surface of clays and soils, Environ. Chem. Lett. 8 (2010) 123–128, https://doi.org/10.1007/s10311-008-0198-2.

[50] G. Roselló-Márquez, R.M. Fernández-Domene, R. Sánchez-Tovar, J. García-Antón, Influence of annealing conditions on the photoelectrocatalytic performance of WO3 nanostructures, Sep. Purif. Technol. 238 (2020), 116417, https://doi.org/10.1016/j.seppur.2019.116417.

[51] E. Sogorb, M.A. Monroy-Noyola, A. Vilanova, The importance of stereospecific hydrolysis in the risk assessment of phosphoramidate insecticides, Rev. Toxicol. 19 (2002) 61–67. http://www.scopus.com/inward/record.url?eid=2-s2.0-00360 71561&partnerID=MN8TOARS.

[52] R.M. Fernández-Domene, R. Sánchez-Tovar, B. Lucas-granados, M.J. Muñoz-Portero, J. García-Antón, Elimination of pesticide atrazine by photoelectrocatalysis using a photoanode based on WO3 nanosheets, Chem. Eng. J. 350 (2018) 1114–1124, https://doi.org/10.1016/j.cej.2018.06.015.

[53] H. Shemer, K.G. Linden, Degradation and by-product formation of diazinon in water during UV and UV/H2O2 treatment, J. Hazard. Mater. 136 (2006) 553–559, https://doi.org/10.1016/j.jhazmat.2005.12.028.

[54] B. Ayoubi-Feiz, M.H. Mashhadizadeh, M. Sheydaei, Preparation of reusable nano N-TiO2/graphene/titanium grid sheet for electrosorption-assisted visible light photoelectrocatalytic degradation of a pesticide: effect of parameters and neural network modeling, J. Electroanal. Chem. 823 (2018) 713–722, https://doi.org/10.1016/j.jelechem.2018.07.020.

[55] D. Churchill, J.M. Dust, E. Buncel, Concerted rate-limiting proton transfer to sulfur with nucleophilic attack at phosphorus - a new proposed mechanism for hydrolytic decomposition of the P═S pesticide, diazinon, in moderately acidic sulfuric acid media, Can. J. Chem. 85 (2007) 421–431, https://doi.org/10.1139/V07-049.

[56] M. Bavcon, P. Trebše, L. Zupančič-Kralj, Investigations of the determination and transformations of diazinon and malathion under environmental conditions using gas chromatography coupled with a flame ionisation detector, Chemosphere 50 (2003) 595–601, https://doi.org/10.1016/S0045-6535(02)00643-4.

[57] R.D. Suryavanshi, S.V. Mohite, A.A. Bagade, K.Y. Rajpure, Photoelectrocatalytic activity of immobilized Fe2O3 photoelectrode for degradation of salicylic acid and methyl orange dye under visible light illumination, Ionics 24 (2018) 1841–1853, https://doi.org/10.1007/s11581-017-2340-2.

[58] D. Vaya, P.K. Surolia, Semiconductor based photocatalytic degradation of pesticides: an overview, Environ. Technol. Innov. 20 (2020), 101128, https://doi.org/10.1016/j.eti.2020.101128.

[59] V. Mahdavi, H. Hamidi, A. Es-haghi, A. Ghassempour, Elucidation of diazinon metabolites in rice plants by liquid chromatography ion-trap mass spectrometry,

Int. J. Environ. Anal. Chem. 98 (2018) 1342–1351, https://doi.org/10.1080/03067319.2018.1554102.

[60] M.D. Perez-Lainez, T. Corona-Torres, M. Del Rosario Garcia-Mateos, R. Winkler, A. F. Barrientos-Priego, R. Nieto-Angel, V.H. Aguilar-Rincon, J.A. Garcia-Velazquez, Metabolomic study of volatile compounds in the pigmented fruit from Mexico crataegus genotypes, J. Appl. Bot. Food Qual. 92 (2019) 15–23, https://doi.org/10.5073/JABFQ.2019.092.003.

[61] V.N. Kouloumbos, D.F. Tsipi, A.E. Hiskia, D. Nikolic, R.B. Van Breemen, Identification of photocatalytic degradation products of diazinon in TiO2 aqueous suspensions using GC/MS/MS and LC/MS with quadrupole time-of-flight mass spectrometry, J. Am. Soc. Mass Spectrom. 14 (2003) 803–817, https://doi.org/10.1016/S1044-0305(03)00333-7.